How does Arbidol Inhibit the Novel Coronavirus SARS-CoV-2? Atomistic Insights from Molecular Dynamics Simulations

Aditya K. Padhi[1], Aniruddha Seal[2,a,b], Timir Tripathi[2,*]

[1]Laboratory for Structural Bioinformatics, Center for Biosystems Dynamics Research, RIKEN, Yokohama, Japan

[2]Molecular and Structural Biophysics Laboratory, Department of Biochemistry, North-Eastern Hill University, Shillong, India

* Corresponding author:

Email: timir.tripathi@gmail.com (TT)

[a]Current Address: School of Chemical Sciences, National Institute of Science Education and Research Bhubaneswar, Khurda, Odisha, India

[b]Homi Bhabha National Institute, Training School Complex, Anushaktinagar, Mumbai, Maharashtra, India

Abstract

The COVID-19 pandemic is spreading at an alarming rate, posing an unprecedented threat to the global economy and human health. Broad-spectrum antivirals are currently being administered for severe acute respiratory syndrome coronavirus 2 (SARS-CoV-2) treatment. China's prevention and treatment guidelines suggest the use of an anti-influenza drug, Arbidol, for the clinical treatment of COVID-19. Reports indicate that Arbidol could neutralize the SARS-CoV-2. Monotherapy with Arbidol is found superior to Lopinavir-Ritonavir or Favipiravir in the treatment of COVID-19. In the SARS-CoV-2, Arbidol acts upon interfering in virus binding to host cells. However, the detailed understanding of Arbidol induced inhibition of SARS-CoV-2 is not known. Here, we present atomistic insights into the Arbidol-induced SARS-CoV-2 membrane fusion inhibition and propose a model of inhibition. Molecular dynamics (MD) simulation-based analyses demonstrate that Arbidol binds and stabilizes at the receptor-binding domain (RBD)/ACE2 interface with a high affinity. It forms stronger intermolecular interactions with RBD than ACE2. Analyses of the detailed decomposition of energy components and binding affinities revealed a substantial increase in the affinity between RBD and ACE2 in the Arbidol-bound RBD/ACE2 complex, suggesting that Arbidol could generate favorable interactions between them. Based on our MD simulation results, we propose that the binding of Arbidol induced structural rigidity in the virus glycoprotein resulting in restriction of the conformational rearrangements associated with membrane attachment and virus entry. Further, key residues of RBD and ACE2 that interacted with Arbidol were identified, opening the doors for the development of therapeutic strategies and higher efficacy Arbidol derivatives or lead drug candidates.

1. Introduction

We are living through an unprecedented existential crisis. The rapid spread of the new coronavirus disease (COVID-19) across all the continents over a short span of a few months has posed a severe global threat. In March 2020, the World Health Organization declared COVID-19 a pandemic, and by early June 2020, COVID-19 had spread to >212 countries, with over 6.5 million confirmed cases and over 380,000 deaths. The causative pathogen of COVID-19, the severe acute respiratory syndrome coronavirus 2 (SARS-CoV-2), represents a great threat to human health and the global economy. Shortly after the outbreak, the genome sequence and organization of the SARS-CoV-2 were determined [1]. SARS-CoV-2 is a large, enveloped, single-positive–strand RNA coronavirus (CoV). The envelope-anchored Spike glycoprotein (S-protein), through binding to the human angiotensin-converting enzyme 2 (ACE2) receptor, facilitates membrane fusion. Upon interaction, the S-protein/ACE2 complex undergoes structural rearrangements that allow the fusion of viral and cellular membranes and entry into host cells.

The receptor-binding domain (RBD) of the S-protein is the central region that is involved in direct interaction with the ACE2 receptor. Several complex structures of RBD/ACE2 have been elucidated, and the interfacial residues have been identified [2, 3]. A cryo-EM structure reveals different conformational states of RBD, namely the active open conformation, the semi-active, and the closed state [3]. Structurally, the SARS-CoV-2 spikes consist of three receptor-binding S1 heads (responsible for receptor recognition), and a trimeric membrane-fusion S2 stalk (responsible for membrane fusion). The S1 is further divided into an N-terminal domain (NTD) and a C-terminal domain (CTD). An extended insertion contains the receptor-binding motif of RBD that contains most interfacial residues. The binding affinity of RBD to ACE2 is the key determinant of SARS-CoV-2 transmissibility. Interestingly, the SARS-CoV-2 RBD displays a stronger affinity for ACE2 compared with the RBD of other CoVs[4], which is attributed to the higher number of residue interaction networks of SARS-CoV-2 with hACE2. Thus, SARS-CoV-2 encodes distinct epitope features in the RBD from other CoVs. The blocking of S-protein to ACE2 receptor interaction and cell fusion is among the key targets for antiviral development [5].

To date, no clinically proven effective antiviral strategy exists for the treatment of COVID-19. Consequently, the management for SARS-CoV-2 is mostly supportive, with only aim to reduce mortality. Clinicians are administering patients with Ritonavir-Lopinavir, hydroxychloroquine, azithromycin, and interleukin-6 inhibitors outside their approved uses and without study protocols, with limited scientific evidence. However, an array of drugs

approved for other viral infections are being studied for the treatment of COVID-19 in hundreds of clinical trials around the globe [6, 7]. For instance, in a preliminary study, an experimental antiviral drug Remdesivir showed a positive effect in diminishing the time to recovery [8]. However, another human trial showed that the drug did not help patients in China with severe COVID-19 [9]. Several clinical trials are also underway to evaluate the suitability and efficacy of other antiviral drugs like Favipiravir, Darunavir, Ribavirin, Galidesivir, Oseltamivir, and Arbidol in the treatment of COVID-19 [10, 11].

Arbidol, also known as Umifenovir, or ethyl-6-bromo-4-[(dimethylamino)methyl]-5-hydroxy-1-methyl-2[(phenylthio)methyl]-indole-3-carboxylate hydrochloride monohydrate, is a small indole derivative. It is a potent broad-spectrum antiviral with proven activity against several enveloped and non-enveloped viruses, including influenza, parainfluenza, corona, polio, Lassa, respiratory syncytial, adenovirus, Coxsackie B5, and hepatitis B and C [12-15]. Arbidol has been used for decades in China and Russia for influenza and other respiratory viral infections and has shown no major adverse effects [12, 13]. It suppresses influenza virus propagation and modulates the expression of inflammatory cytokines *in vitro* and *in vivo* [16]. Currently, Arbidol is recommended by China's prevention and treatment guidelines and used in the clinical treatment of COVID-19. Arbidol interferes with multiple stages of the virus life cycle; by directly targeting viral proteins or virus-associated host factors [12]. In the influenza virus, Arbidol binds to hemagglutinin (HA), the major cell-surface glycoprotein, and prevents the fusion of the viral membrane [17]. A recent study reveals that Arbidol efficiently inhibits SARS-CoV-2 infection. Arbidol blocks both viral entry (by interfering virus binding to host cells) and post-entry stages (by blocking intracellular vesicle trafficking) [18]. However, how the Arbidol modulates RBD/ACE2 interaction is not completely elucidated, thereby obscuring its development as a specific therapeutic for COVID-19. Thus, we aimed to investigate the molecular basis underlying the RBD/ACE2 interaction inhibition using all-atom molecular dynamics (MD) simulations. Our data provide details on why Arbidol is effective against SARS-CoV-2. The understanding gained from this study would be useful for the design and development of more specific SARS-CoV-2 inhibitors.

2. Methods

2.1. System preparation and molecular docking simulations

The co-crystal structure of the SARS-CoV-2 RBD/ACE2 complex was retrieved from the RCSB Protein Data Bank (PDB ID: 6LZG) and used for docking (Fig 1A) [19]. The

molecular docking was carried out with Arbidol (Umifenovir) [PubChem ID: 131411] (Fig 1B). The CB-Dock protein-ligand docking method was used for the docking of Arbidol with ACE2 and RBD separately, and into the RBD/ACE2 complex. This method automatically identifies the binding sites, calculates the center and size, customizes the docking box size according to the query ligands, and then performs the molecular docking with AutoDock Vina [20]. To start with, the Arbidol was docked to ACE2 and RBD separately, and into the RBD/ACE2 complex. Arbidol was found to bind to several positions in all three conditions. However, Since Arbidol inhibits the SARS-CoV-2 membrane attachment to host cells, Arbidol was docked into the RBD/ACE2 complex structure. During this process, twenty cavities were generated and used, and molecular docking was performed at each of the cavities. The binding modes were analyzed *in cerebro*, and the docked pose with the highest AutoDock Vina score and cavity size was selected for subsequent experiments.

2.2. Molecular dynamics (MD) simulations

The selected docked complex of RBD/ACE2-Arbidol was prepared using Schrödinger Maestro (Schrödinger Release 2016–4: Maestro, Schrödinger, New York) and subsequently used for MD simulations. As a first step, the topology of Arbidol was generated using Automated Topology Builder and Repository, and the resulting complex was subjected to the addition of hydrogen atoms[21, 22]. Next, the complex was solvated in a dodecahedron box of a simple point charge (SPC) water in the center at least 1.0 nm from the box edge [23]. Appropriate counterions were then added to neutralize the system electrostatically. MD simulations for the resulting system were carried out using the GROMACS 5.1.2 software package with gromos96 54A7 forcefield [24-26]. The system was subjected to 50,000 steps of energy minimization until the energy was stabilized, followed by a heating step from 0 to 300K in 200 picoseconds (ps) and a constant temperature equilibration for 1000 ps at 300K. In the equilibration stage, the impact of velocity was prevented by employing the Parrinello-Rahman barostat pressure coupling [27]. After monitoring the convergence of the complex, a 300 nanosecond (ns) production run was performed with periodic boundary conditions in the NPT ensemble, where a modified Berendsen temperature coupling and a constant pressure of 1 atm was employed [28]. In this process, the LINCS algorithm, along with the Particle-mesh Ewald method, was used for the calculation of long-range electrostatic forces [29, 30]. During the simulation, the Fourier grid spacing and Coulomb radius were set at 0.16 and 1.4 nm, respectively, and the van der Waals interactions were limited to 1.4 nm. The MD trajectories were saved at every 10 ps for energy stabilization, and the root mean square

deviation (RMSD) calculations. As a control experiment, to understand the dynamics between RBD/ACE2 in the absence of Arbidol, the simulation for the apo system was carried out under similar conditions for 300 ns. From here onwards, the RBD/ACE2 complex without Arbidol will be termed as apo-RBD/ACE2 complex, and the RBD/ACE2 complex bound to Arbidol will be termed as RBD/ACE2-Arbidol complex.

2.3. Analysis from MD simulations

The MD simulated trajectory was analyzed using gmx rms, gmx rmsf, and gmx gyrate GROMACS utilities to obtain the RMSD, root mean square fluctuation (RMSF), and radius of gyration (Rg) of each system respectively. Hydrogen bonds were computed using the hydrogen bonds plug-in of visual molecular dynamics (VMD) [31].

2.4. Essential dynamics of the Apo and RBD/ACE2-Arbidol complex

To understand the dominant and collective modes from the overall dynamics of the MD trajectory for the apo-RBD/ACE2 complex and the RBD/ACE2-Arbidol complex, principal component analysis (PCA) and essential dynamics was performed, where a variance/covariance matrix was constructed by calculating the eigenvectors and eigenvalues and their projection along with the first two principal components (PCs) by essential dynamics [32]. The movements of the complexes in the essential subspace were identified by projecting the Cartesian trajectory coordinates along the important eigenvectors. The eigenvalues associated with each eigenvector of the complexes were used to calculate the percentage of variability. The GROMACS built-in gmx covar and gmx anaeig modules were used to obtain the eigenvalues and eigenvectors by calculating and diagonalizing the covariance matrix. To study the conformational changes in the apo-RBD/ACE2 complex and the RBD/ACE2-Arbidol complex, the free energy landscape was computed by the gmx sham package [33, 34].

2.5. Binding free energy calculations

For calculating the binding free energies between the complexes- RBD-Arbidol, ACE2-Arbidol, and RBD-ACE2-Arbidol, molecular mechanics/Poisson Boltzmann surface area (MM-PBSA) methodology employed in the g_mmpbsa tool of GROMACS was used [35, 36]. In MM-PBSA, the binding free energy of the protein and ligand is typically defined as

$$\Delta Gbinding = \Delta Gcomplex - (\Delta Gprotein + \Delta Gligand)$$

where $\Delta G_{complex}$, $\Delta G_{protein}$, and ΔG_{ligand} represent the total free energies of the protein, the ligand, and the protein-ligand complex, separately in the solvent, respectively [37, 38]. In general, the free energy of the individual entity is represented as

$$G = EMM + Gsolvation - TS$$

where E_{MM} represents the average molecular mechanics potential energy in the vacuum, $G_{solvation}$ denotes the free energy of solvation, and TS represents the entropic contribution to the free energy in a vacuum, where T and S denote the temperature and entropy, respectively. Further, the E_{MM} comprises bonded and nonbonded terms, including bond angle, torsion, and electrostatic (E_{elec}) and the van der Walls (E_{vdw}) interactions, respectively. Lastly, the solvation free energy, $G_{solvation}$ considers both electrostatic and non-electrostatic (G_{polar} and $G_{nonpolar}$) components. The binding free energy of RBD-Arbidol, ACE2-Arbidol, and RBD-ACE2 complexes were calculated for 200 snapshots obtained from the last 30 ns of the trajectories.

2.6. Interaction network of RBD/ACE2-Arbidol and Binding affinity calculations using PRODIGY- and PPCheck-protocols

Representative structures of the RBD/ACE2-Arbidol complex were extracted from the last 30 ns of the stabilized MD simulated trajectory, and all the intermolecular interactions between Arbidol with RBD/ACE2 were computed using Schrödinger Maestro. The binding affinity between RBD/ACE2 and RBD/ACE2-Arbidol complex structures were first computed using PROtein binDIng enerGY prediction (PRODIGY), a predictor of binding affinity in a protein-protein and protein-ligand complex[39-42]. In this method, after the 3D model is supplied with a suitable temperature (default of 25°C), the binding affinity is computed. PPCheck was used to quantify the strength of a protein-protein interface, where the structures of apo-RBD/ACE2 complex and RBD/ACE2-Arbidol complex structures extracted from MD simulations were used to calculate the interaction energies and total stabilizing energy [43]. The total stabilizing energy (Et) is a summation of energy values for all the nonbonded interactions that include van der Waals interactions, electrostatic interactions, and hydrogen bond interactions. Besides, it also computes the number of short contacts, hydrophobic interactions, van der Waals pairs, salt bridges, potential favorable electrostatic interactions, and potential unfavorable electrostatic interactions in the interface, thus providing comprehensive knowledge on qualitative and quantitative features between the RBD/ACE2 with or without Arbidol binding.

2.7. Figures and rendering

Figures were rendered and generated using PyMOL and VMD. Ligand interaction diagrams were generated using Schrödinger Maestro (Schrödinger Release 2016–4: Maestro, Schrödinger, New York).

3. Results

3.1. Molecular docking of Arbidol into ACE2-RBD complex

Arbidol inhibits the SARS-CoV-2 membrane fusion to host cells, suggesting that it targets the S-protein/ACE2 interactions. Since the RBD of S-protein is involved in ACE2 recognition, Arbidol was docked into the RBD/ACE2 complex structure. First, when Arbidol was docked into ACE2 and RBD separately, it was not docked at the ACE2 and RBD binding interface (S1 Fig). Moreover, the largest cavities where the Arbidol was docked were not at the interface of the RBD side (facing ACE2) or ACE2 side (facing RBD) (S1 Fig). Following this, when Arbidol was docked into the RBD/ACE2 complex, it quickly docked into one of the largest cavities in the RBD/ACE2 interface with a high score [cavity size: 940, center: 176*114*247 (x*y*z) and size: 22*22*22 (x*y*z)]. It was found that Arbidol binds and stabilizes at the RBD/ACE2 interface with a high binding affinity (AutoDock Vina score of -5.7) (Fig 2). The docked complex was subsequently used for studying detailed structural, dynamics, and binding mechanisms to understand how it targets the RBD/ACE2 interface.

3.2. Stability of RBD/ACE2-Arbidol complex during MD simulations

The MD simulation trajectories comprising 300 ns of independent simulations for the apo-RBD/ACE2 complex and the RBD/ACE2-Arbidol complex were examined for their structural and dynamic behavior. The root-mean square deviation (RMSD) of the backbone atoms computed over 300 ns revealed that the apo-RBD/ACE2 complex reached the stability after about 75 ns, whereas the RBD/ACE2-Arbidol complex took nearly 125 ns to converge (Fig 3A). Beyond 125 ns, both the systems were stabilized till the end of the production run and converged overall; however, the RMSD profiles suggested that the last 30 ns were most preferable for further structural and dynamics analyses. The analysis of hydrogen bonds formed for the apo-RBD/ACE2 complex and the RBD/ACE2-Arbidol complex revealed that upon binding of Arbidol, the RBD/ACE2 complex was able to form a higher number of hydrogen bond interactions as compared to the apo-RBD/ACE2 complex (Fig 3B). While the apo-RBD/ACE2 complex formed an average of 188 hydrogen bond interactions, the RBD/ACE2-Arbidol complex formed 247 hydrogen bond interactions on average during the

300 ns simulations (Fig 3B). This indicated that the hydrogen bonds probably play an essential role in stabilizing the RBD/ACE2-Arbidol complex during the simulation and confer stability to the RBD/ACE2-Arbidol complex.

3.3. Structural flexibility and compactness of the RBD/ACE2-Arbidol complex

The structural flexibility of the apo-RBD/ACE2 complex and Arbidol bound complex was evaluated by computing the per-residue root mean square fluctuations (RMSF). It was observed that, as expected, the RBD/ACE2-Arbidol complex exhibited an overall lower RMSF as compared to the apo-RBD/ACE2 complex (Fig 3C). While the apo-RBD/ACE2 complex showed an average RMSF of 2.49 Å, the RBD/ACE2-Arbidol complex showed a lower 1.67 Å average RMSF during the simulation, corroborating with the RMSD and hydrogen bonds interaction profiles (Fig 3C). We were then curious to investigate how the two molecular systems displayed their compactness during the simulations. For this, we computed the Rg for both complexes over the 300 ns. It was evident from the Rg profiles that the RBD/ACE2-Arbidol complex exhibited a more compact behavior as compared to the apo-RBD/ACE2 complex (Fig 3D). The average Rg was found to be 5.29 Å, and 3.27 Å for the apo-RBD/ACE2 complex and RBD/ACE2-Arbidol complex, respectively. Interestingly, the Rg profile of the RBD/ACE2-Arbidol complex was found to be more stable than the apo-RBD/ACE2 complex. All these data indicate that the formation of more hydrogen bonds, reduced per-residue fluctuation, and higher compactness in the RBD/ACE2-Arbidol complex drive its overall stability and convergence.

3.4. Principal component and Free energy analysis of RBD/ACE2-Arbidol complex

Principal component analysis (PCA) is an important technique that can provide insights into the correlation of atomic movement of enzyme and substrate interactions, raised from the collective motion of atoms that are controlled by the secondary structure of the proteins. Typically, the largest associated eigenvalues define the essential subspace in which most of the protein dynamics occur. For this, the clusters of stable states of PCA for the apo-RBD/ACE2 complex and RBD/ACE2-Arbidol complex were visualized and analyzed (S2 Fig). The trace values calculated from the covariance matrix of the apo-RBD/ACE2 complex and RBD/ACE2-Arbidol complex were found to be 80.76 nm^2 and 69.51 nm^2 respectively, suggesting that the RBD/ACE2 complex gained compaction upon binding of Arbidol. On the other hand, a higher trace value of the apo-RBD/ACE2 complex suggested a comparatively high flexible behavior. It was also observed that the majority of the dynamics that occurred

were contributed by a small number of eigenvectors representing the overall collective motions. Next, the Gibbs free energy landscape (FEL) plot was generated using the PC1 and PC2 coordinates. In the FEL plots, the ΔG value of apo-RBD/ACE2 complex and RBD/ACE2-Arbidol complex ranged between 0-15.8 kJ/mol (Fig 4).

3.5. Binding free energy calculations between ACE2-Arbidol and RBD-Arbidol

To investigate how strongly Arbidol binds with ACE2 and RBD, and the associated binding modes, the binding free energies were computed using the MM-PBSA method. For this, the last 30 ns of the MD simulation trajectories were investigated to obtain the binding affinities and insights into the binding mechanisms of Arbidol. It was observed that the Arbidol displayed a binding affinity of -169.66 kJ/mol with ACE2 (Table 1). Detailed decomposition of energy components revealed that except the polar solvation energy, the van der Waals energy, electrostatic energy, and the SASA energy, all contributed to the tighter binding of Arbidol with ACE2. When the binding affinity of Arbidol was computed against RBD, it was found that Arbidol exhibited an even higher affinity of -194.16 kJ/mol with RBD than with ACE2 (Table 1). An energy decomposition profile further revealed similar energy components to that of ACE2; however, the van der Waals energy and electrostatic energy were found to be positively contributing towards tighter binding with RBD. An interaction diagram from an average structure obtained from the MD simulations supported the binding mechanism of the Arbidol to RBD/ACE2 complex (Fig 5A). Additionally, the well-superposed structures of Arbidol in the RBD/ACE2 interface obtained from the last 30 ns simulation further confirmed the stability and preferred mechanism of binding (Fig 5B). From the detailed binding free energy calculations and visual assessment, it can be concluded that Arbidol has a higher binding affinity towards RBD, probably due to the establishment of a higher number of favorable interactions with surrounding key residues.

3.6. Key residues governing the binding of Arbidol to ACE2 and RBD

Following the estimation of binding affinities of Arbidol towards ACE2 and RBD, we identified the critical residues of ACE2 and RBD that positively and negatively impacted the binding of Arbidol. First, the contribution energy of individual interacting residues of ACE2 revealed that residues Leu320, Pro321, Met383, Ala384, and Phe555 contributed the most towards the affinity of ACE2 towards Arbidol (Fig 6A). On the other hand, Arbidol established an even higher binding affinity towards the RBD, where many residues positively contributed towards its tighter binding. It was found that an array of residues such as Thr376,

Tyr380, Ile402, Val407, Val433, Ala435, Ala475, Val503, and Val510 contributed towards the higher binding of RBD towards Arbidol (Fig 6B). Interestingly, they were also found to be a part of ACE2-RBD interface interacting residues, which further confirms that Arbidol binds and inhibits the interfacial residues of ACE2/RBD complex, where it established more contacts and interactions with the RBD as compared to the ACE2 receptor. Further, to understand the intermolecular interactions between Arbidol and ACE2/RBD complex, representative structures were extracted from the MD simulation trajectory and analyzed using Schrödinger Maestro. It was found that while Arbidol established few intermolecular interactions with residues of ACE2, it formed a relatively higher number of crucial interactions with RBD (S3 Fig). Overall, the analysis of the RBD/ACE2-Arbidol complex interactions provided information on the vital residue interactions and gave the insights to explore the differences between ACE2-Arbidol and RBD-Arbidol binding and its inhibitory mechanism.

3.7. Intermolecular interactions and energy components between ACE2 and RBD upon Arbidol binding

Next, we computed the binding affinity using PRODIGY for the apo-RBD/ACE2 complex and the RBD/ACE2-Arbidol complex extracted from MD simulations. We found that the RBD/ACE2-Arbidol complex exhibited a higher binding affinity (ΔG) of -11.5 kcal/mol, whereas the apo-RBD/ACE2 complex exhibited a relatively lower binding affinity (ΔG) of -10.8 kcal/mol. We observed that the higher binding affinity in the RBD/ACE2-Arbidok complex was due to an increase in the number of intermolecular, charged-polar, charged-apolar, and apolar-apolar contacts. The detailed decomposition of intermolecular contacts governing the difference in binding energies is shown in Table 2. PPCheck was also used to compute the total stabilizing energy and the types of interactions in the apo-RBD/ACE2 complex and RBD/ACE2-Arbidol complex, extracted from MD simulations. It was observed that the total stabilizing energy for the apo-RBD/ACE2 complex was -113.46 kJ/mol, whereas, for the RBD/ACE2-Arbidol complex, it was -171.57 kJ/mol (Table 3). A closer inspection of interactions and energy components revealed that the hydrogen bonds and van der Waals pairs contributing to hydrogen bond energy and van der Waals energy largely governed the difference in total stabilizing energy and between the affinity of the RBD/ACE2 complex in its apo-RBD/ACE2 complex and RBD/ACE2-Arbidol complex (Table 3).

4. Discussion

The COVID-19 pandemic heightens the need for preparedness to respond to emerging virus threats rapidly. No therapies have been shown clinically effective to date. To assist the efforts to control the rapidly evolving pandemic, drug repurposing is being employed as an effective and fast method. Given the urgency of the situation, it is vital that scientists could understand and characterize the molecular mechanisms of action of repurposed drugs being tested for COVID-19 treatment. Computational understanding of molecular mechanisms of unproven anti-COVID-19 drugs may guide scientists towards developing a specific therapeutic against SARS-CoV-2.

Arbidol, a broad-spectrum antiviral drug, is currently being used as a standard treatment option for COVID-19 [44-47]. It shows significant antiviral and anti-inflammatory efficacy both *in vitro* and *in vivo* against the influenza virus [16]. Since SARS-CoV-2 and influenza viruses exhibit similar disease pathology, it is expected that Arbidol could present an anti-SARS-CoV-2 activity. Arbidol is patented for its medicinal use as an antiviral agent against atypical pneumonia induced by the SARS-CoV (http://www.arbidol.org/arbidol-patent-2004-sars-russian.pdf). It has been found to effectively inhibit SARS-CoV-2 at a concentration of 4.11 µM *in vitro,* suggesting its potential in the treatment of COVID-19 patients [18]. Presently, at least four clinical trials are being conducted with Arbidol as a single agent for COVID-19 treatment [48-51]. A few case reports showed that patients with COVID-19 successfully recovered after receiving Arbidol and Lopinavir/Ritonavir therapy [48, 52, 53]. Arbidol has been shown to be superior to the antiviral Favipiravir, which did not improve the clinical recovery rate of Day 7 compared to the Arbidol group [54]. A recent result of a clinical trial in China indicated that Arbidol monotherapy is also superior to Lopinavir/Ritonavir in treating COVID-19 [55]. A study with a small sample size report that Arbidol could not improve the prognosis of COVID-19 in non-ICU patients; however, their study was preliminary and limited by several factors as the research was, i) a single-center and retrospective study, ii) pharyngeal swabs were not collected every day, and iii) only included patients with moderate and severe COVID-19, so the efficacy of Arbidol in mild and critical patients could not be confirmed[56]. Arbidol binds to the interface of viral glycoprotein and human cell surface receptors, thereby blocking membrane fusion and viral entry [13, 57-59]. The binding of Arbidol is topologically away from the active site of the ACE2 receptor. In SARS-CoV-2, Arbidol acts upon interfering in virus binding to host cells [18]. A few molecular docking studies of Arbidol against the SARS-CoV2 RBD and human ACE2 complex have revealed specific residues involved in the interaction; however, the

detailed mechanism underlying the process and the associated dynamics are not known [60, 61].

Our analyses of the 300 ns MD simulation trajectories revealed that when Arbidol was docked into the RBD-ACE2 complex interface, it stabilized and formed favorable interactions with both RBD and ACE2 proteins. However, Arbidol displayed a higher binding affinity to RBD than ACE2. The analysis of hydrogen bonds revealed that upon binding of Arbidol, the RBD/ACE2 complex could form a higher number of hydrogen bond interactions as compared to the apo-RBD/ACE2 complex. The binding also induced structural rigidity and compaction in the RBD/ACE2-Arbidol complex. The compaction was also confirmed by the PCA analyses, where the RBD/ACE2-Arbidol complex formed a more stable cluster. Detailed decomposition of energy components revealed that the binding of Arbidol to ACE2 is due to positive contributions from the van der Waals energy, electrostatic energy, and the SASA energy, while the tighter binding of Arbidol to RBD is mainly due to positive contributions from the van der Waals energy and electrostatic energy. Further, Arbidol binding leads to a substantial increase in the binding affinity between RBD and ACE2, indicating that Arbidol induces favorable interactions between them. During the simulations, RBD remained bound to ACE2; however, substantial conformational rearrangements occurred to both partner proteins, the ACE2, and the RBD (the loop between β6 and β7; residues S477 to G485). Overall, the data indicated that Arbidol binding drives the increase in structural stability, compactness, and convergence of the RBD/ACE2 complex. In the absence of any Arbidol-bound complex structure of RBD/ACE2 complex, the data offer to hypothesize that Arbidol binding to the interface of viral glycoprotein and human receptors induces structural rigidity leading to inhibition of the conformational changes in the S-protein that is associated during the virus entry. The understanding gained from this study would be useful for the design and development of more specific SARS-CoV-2 inhibitors.

Authors' contributions

AKP carried out the experiments and data generation. AKP, AS, and TT conceived the study. AKP and TT participated in its design and coordination. AKP and TT analyzed the data and drafted the manuscript. All authors read and approved the final manuscript.

References

1. Lu R, Zhao X, Li J, Niu P, Yang B, Wu H, et al. Genomic characterisation and epidemiology of 2019 novel coronavirus: implications for virus origins and receptor binding. Lancet. 2020;395(10224):565-74. Epub 2020/02/03. doi: 10.1016/s0140-6736(20)30251-8. PubMed PMID: 32007145; PubMed Central PMCID: PMCPMC7159086.

2. Lan J, Ge J, Yu J, Shan S, Zhou H, Fan S, et al. Structure of the SARS-CoV-2 spike receptor-binding domain bound to the ACE2 receptor. Nature. 2020;581(7807):215-20. Epub 2020/04/01. doi: 10.1038/s41586-020-2180-5. PubMed PMID: 32225176.

3. Wrapp D, Wang N, Corbett KS, Goldsmith JA, Hsieh CL, Abiona O, et al. Cryo-EM structure of the 2019-nCoV spike in the prefusion conformation. Science. 2020;367(6483):1260-3. Epub 2020/02/23. doi: 10.1126/science.abb2507. PubMed PMID: 32075877; PubMed Central PMCID: PMCPMC7164637.

4. Tai W, He L, Zhang X, Pu J, Voronin D, Jiang S, et al. Characterization of the receptor-binding domain (RBD) of 2019 novel coronavirus: implication for development of RBD protein as a viral attachment inhibitor and vaccine. Cellular & Molecular Immunology. 2020;17(6):613-20. doi: 10.1038/s41423-020-0400-4.

5. Zhou Y, Hou Y, Shen J, Huang Y, Martin W, Cheng F. Network-based drug repurposing for novel coronavirus 2019-nCoV/SARS-CoV-2. Cell Discov. 2020;6(1):14. doi: 10.1038/s41421-020-0153-3.

6. Gordon DE, Jang GM, Bouhaddou M, Xu J, Obernier K, White KM, et al. A SARS-CoV-2 protein interaction map reveals targets for drug repurposing. Nature. 2020. doi: 10.1038/s41586-020-2286-9.

7. Guy RK, DiPaola RS, Romanelli F, Dutch RE. Rapid repurposing of drugs for COVID-19. Science. 2020;368(6493):829. doi: 10.1126/science.abb9332.

8. Beigel JH, Tomashek KM, Dodd LE, Mehta AK, Zingman BS, Kalil AC, et al. Remdesivir for the Treatment of Covid-19 - Preliminary Report. N Engl J Med. 2020. Epub 2020/05/24. doi: 10.1056/NEJMoa2007764. PubMed PMID: 32445440.

9. Wang Y, Zhang D, Du G, Du R, Zhao J, Jin Y, et al. Remdesivir in adults with severe COVID-19: a randomised, double-blind, placebo-controlled, multicentre trial. The Lancet. 2020;395:1569–78. doi: 10.1016/S0140-6736(20)31022-9.

10. Dong L, Hu S, Gao J. Discovering drugs to treat coronavirus disease 2019 (COVID-19). Drug Discov Ther. 2020;14(1):58-60. Epub 2020/03/10. doi: 10.5582/ddt.2020.01012. PubMed PMID: 32147628.

11. Tu YF, Chien CS, Yarmishyn AA, Lin YY, Luo YH, Lin YT, et al. A Review of SARS-CoV-2 and the Ongoing Clinical Trials. Int J Mol Sci. 2020;21(7). Epub 2020/04/16. doi: 10.3390/ijms21072657. PubMed PMID: 32290293; PubMed Central PMCID: PMCPMC7177898.

12.	Blaising J, Polyak SJ, Pecheur EI. Arbidol as a broad-spectrum antiviral: an update. Antiviral Res. 2014;107:84-94. Epub 2014/04/29. doi: 10.1016/j.antiviral.2014.04.006. PubMed PMID: 24769245; PubMed Central PMCID: PMCPMC7113885.

13.	Boriskin YS, Leneva IA, Pecheur EI, Polyak SJ. Arbidol: a broad-spectrum antiviral compound that blocks viral fusion. Curr Med Chem. 2008;15(10):997-1005. Epub 2008/04/09. doi: 10.2174/092986708784049658. PubMed PMID: 18393857.

14.	Herod MR, Adeyemi OO, Ward J, Bentley K, Harris M, Stonehouse NJ, et al. The broad-spectrum antiviral drug arbidol inhibits foot-and-mouth disease virus genome replication. J Gen Virol. 2019;100(9):1293-302.

15.	Pecheur EI, Borisevich V, Halfmann P, Morrey JD, Smee DF, Prichard M, et al. The Synthetic Antiviral Drug Arbidol Inhibits Globally Prevalent Pathogenic Viruses. J Virol. 2016;90(6):3086-92. doi: 10.1128/JVI.02077-15.

16.	Wang Y, Ding Y, Yang C, Li R, Du Q, Hao Y, et al. Inhibition of the infectivity and inflammatory response of influenza virus by Arbidol hydrochloride in vitro and in vivo (mice and ferret). Biomed Pharmacother. 2017;91:393-401. Epub 2017/05/06. doi: 10.1016/j.biopha.2017.04.091. PubMed PMID: 28475918.

17.	Kadam RU, Wilson IA. Structural basis of influenza virus fusion inhibition by the antiviral drug Arbidol. Proc Natl Acad Sci U S A. 2017;114(2):206-14. Epub 2016/12/23. doi: 10.1073/pnas.1617020114. PubMed PMID: 28003465; PubMed Central PMCID: PMCPMC5240704.

18.	Wang X, Cao R, Zhang H, Liu J, Xu M, Hu H, et al. The anti-influenza virus drug, arbidol is an efficient inhibitor of SARS-CoV-2 in vitro. Cell Discov. 2020;6:28.

19.	Wang Q, Zhang Y, Wu L, Niu S, Song C, Zhang Z, et al. Structural and Functional Basis of SARS-CoV-2 Entry by Using Human ACE2. Cell. 2020;181(4):894-904.e9. Epub 2020/04/11. doi: 10.1016/j.cell.2020.03.045. PubMed PMID: 32275855; PubMed Central PMCID: PMCPMC7144619.

20.	Liu Y, Grimm M, Dai WT, Hou MC, Xiao ZX, Cao Y. CB-Dock: a web server for cavity detection-guided protein-ligand blind docking. Acta Pharmacol Sin. 2020;41(1):138-44. Epub 2019/07/03. doi: 10.1038/s41401-019-0228-6. PubMed PMID: 31263275.

21.	Koziara KB, Stroet M, Malde AK, Mark AE. Testing and validation of the Automated Topology Builder (ATB) version 2.0: prediction of hydration free enthalpies. J Comput Aided Mol Des. 2014;28(3):221-33. Epub 2014/01/31. doi: 10.1007/s10822-014-9713-7. PubMed PMID: 24477799.

22.	Malde AK, Zuo L, Breeze M, Stroet M, Poger D, Nair PC, et al. An Automated Force Field Topology Builder (ATB) and Repository: Version 1.0. J Chem Theory Comput. 2011;7(12):4026-37. Epub 2011/12/13. doi: 10.1021/ct200196m. PubMed PMID: 26598349.

23.	Berendsen HJC, Postma JPM, van Gunsteren WF, Hermans J. Interaction Models for Water in Relation to Protein Hydration. In: Pullman B, editor. Intermolecular Forces: Proceedings of the Fourteenth Jerusalem Symposium on Quantum Chemistry and Biochemistry Held in Jerusalem, Israel, April 13–16, 1981. Dordrecht: Springer Netherlands; 1981. p. 331-42.

24.	Huang W, Lin Z, van Gunsteren WF. Validation of the GROMOS 54A7 Force Field with Respect to β-Peptide Folding. J Chem Theory Comput. 2011;7(5):1237-43. Epub 2011/05/10. doi: 10.1021/ct100747y. PubMed PMID: 26610119.

25.	Schmid N, Eichenberger AP, Choutko A, Riniker S, Winger M, Mark AE, et al. Definition and testing of the GROMOS force-field versions 54A7 and 54B7. Eur Biophys J. 2011;40(7):843-56. Epub 2011/05/03. doi: 10.1007/s00249-011-0700-9. PubMed PMID: 21533652.

26.	Liu H, Mark AE, van Gunsteren WF. Estimating the relative free energy of different molecular states with respect to a single reference state. J Phys Chem B. 1996;100(22):9485-94.

27.	Parrinello M, Rahman A. Polymorphic transitions in single crystals: A new molecular dynamics method. . J Appl Phys. 1981;52:7182-90.

28.	Berendsen HJ, Postma J, van Gunsteren WF, DiNola A, Haak JR. Molecular dynamics with coupling to an external bath. J Appl Phys. 1984;81:3684-90.

29.	Darden T, York D, Pedersen L. Particle mesh Ewald: An N· log (N) method for Ewald sums in large systems. . J Chem Phys. 1993;98:10089-92.

30.	Hess B, Bekker H, Berendsen HJ, Fraaije JG. LINCS: a linear constraint solver for molecular simulations. J Comput Chem. 1997;18:1463-72

31.   Humphrey W, Dalke A, Schulten K. VMD: visual molecular dynamics. J Mol Graph. 1996;14(1):33-8, 27-8. Epub 1996/02/01. doi: 10.1016/0263-7855(96)00018-5. PubMed PMID: 8744570.

32.   Amadei A, Linssen AB, Berendsen HJ. Essential dynamics of proteins. Proteins. 1993;17(4):412-25. Epub 1993/12/01. doi: 10.1002/prot.340170408. PubMed PMID: 8108382.

33.   Brooks CL, 3rd, Onuchic JN, Wales DJ. Statistical thermodynamics. Taking a walk on a landscape. Science. 2001;293(5530):612-3. Epub 2001/07/28. doi: 10.1126/science.1062559. PubMed PMID: 11474087.

34.   Mitsutake A, Sugita Y, Okamoto Y. Generalized-ensemble algorithms for molecular simulations of biopolymers. Biopolymers. 2001;60(2):96-123. Epub 2001/07/17. doi: 10.1002/1097-0282(2001)60:2<96::Aid-bip1007>3.0.Co;2-f. PubMed PMID: 11455545.

35.   Homeyer N, Gohlke H. Free Energy Calculations by the Molecular Mechanics Poisson-Boltzmann Surface Area Method. Mol Inform. 2012;31(2):114-22. Epub 2012/02/01. doi: 10.1002/minf.201100135. PubMed PMID: 27476956.

36.   Kumari R, Kumar R, Lynn A. g_mmpbsa--a GROMACS tool for high-throughput MM-PBSA calculations. J Chem Inf Model. 2014;54(7):1951-62. Epub 2014/05/23. doi: 10.1021/ci500020m. PubMed PMID: 24850022.

37.   Gohlke H, Kiel C, Case DA. Insights into protein-protein binding by binding free energy calculation and free energy decomposition for the Ras-Raf and Ras-RalGDS complexes. J Mol Biol. 2003;330(4):891-913. Epub 2003/07/10. doi: 10.1016/s0022-2836(03)00610-7. PubMed PMID: 12850155.

38.   Wang W, Kollman PA. Free energy calculations on dimer stability of the HIV protease using molecular dynamics and a continuum solvent model. J Mol Biol. 2000;303(4):567-82. Epub 2000/10/31. doi: 10.1006/jmbi.2000.4057. PubMed PMID: 11054292.

39.   Vangone A, Bonvin AM. Contacts-based prediction of binding affinity in protein-protein complexes. Elife. 2015;4:e07454. Epub 2015/07/21. doi: 10.7554/eLife.07454. PubMed PMID: 26193119; PubMed Central PMCID: PMCPMC4523921.

40.   Xue LC, Rodrigues JP, Kastritis PL, Bonvin AM, Vangone A. PRODIGY: a web server for predicting the binding affinity of protein-protein complexes. Bioinformatics. 2016;32(23):3676-8. Epub 2016/08/10. doi: 10.1093/bioinformatics/btw514. PubMed PMID: 27503228.

41.   Vangone A, Schaarschmidt J, Koukos P, Geng C, Citro N, Trellet ME, et al. Large-scale prediction of binding affinity in protein-small ligand complexes: the PRODIGY-LIG web server. Bioinformatics. 2019;35(9):1585-7. Epub 2019/05/06. doi: 10.1093/bioinformatics/bty816. PubMed PMID: 31051038.

42.   Kurkcuoglu Z, Koukos PI, Citro N, Trellet ME, Rodrigues J, Moreira IS, et al. Performance of HADDOCK and a simple contact-based protein-ligand binding affinity predictor in the D3R Grand Challenge 2. J Comput Aided Mol Des. 2018;32(1):175-85. Epub 2017/08/24. doi: 10.1007/s10822-017-0049-y. PubMed PMID: 28831657; PubMed Central PMCID: PMCPMC5767195.

43.   Sukhwal A, Sowdhamini R. Oligomerisation status and evolutionary conservation of interfaces of protein structural domain superfamilies. Mol Biosyst. 2013;9(7):1652-61. Epub 2013/03/28. doi: 10.1039/c3mb25484d. PubMed PMID: 23532342.

44.   Anonymous. Chinese Clinical Guidance for COVID-19 Pneumonia Diagnosis and Treatment. In: Cardiology CSo, editor. 7th edition ed. China: China National Health Commission; 2020.

45.   Hulseberg CE, Feneant L, Szymanska-de Wijs KM, Kessler NP, Nelson EA, Shoemaker CJ, et al. Arbidol and Other Low-Molecular-Weight Drugs That Inhibit Lassa and Ebola Viruses. J Virol. 2019;93(8). Epub 2019/02/01. doi: 10.1128/jvi.02185-18. PubMed PMID: 30700611; PubMed Central PMCID: PMCPMC6450122.

46.   Pei-Fang W. Diagnosis and Treatment Protocol for Novel Coronavirus Pneumonia (Trial Version 7). Chin Med J (Engl). 2020;133(9):1087-95. Epub 2020/05/03. doi: 10.1097/cm9.0000000000000819. PubMed PMID: 32358325.

47.   Pshenichnaya NY, Bulgakova VA, Lvov NI, Poromov AA, Selkova EP, Grekova AI, et al. Clinical efficacy of umifenovir in influenza and ARVI (study ARBITR). Ter Arkh. 2019;91(3):56-63. Epub 2019/05/17. doi: 10.26442/00403660.2019.03.000127. PubMed PMID: 31094461.

48.   The Efficacy of Lopinavir Plus Ritonavir and Arbidol Against Novel Coronavirus Infection. https://ClinicalTrials.gov/show/NCT04252885.

49.   Clinical Study of Arbidol Hydrochloride Tablets in the Treatment of Pneumonia Caused by Novel Coronavirus. https://ClinicalTrials.gov/show/NCT04260594.

50.   A Prospective/Retrospective, Randomized Controlled Clinical Study of Antiviral Therapy in the 2019-nCoV Pneumonia. https://ClinicalTrials.gov/show/NCT04255017.

51.   The Clinical Study of Carrimycin on Treatment Patients With COVID-19. https://ClinicalTrials.gov/show/NCT04286503.

52.   Lim J, Jeon S, Shin HY, Kim MJ, Seong YM, Lee WJ, et al. Case of the Index Patient Who Caused Tertiary Transmission of COVID-19 Infection in Korea: the Application of Lopinavir/Ritonavir for the Treatment of COVID-19 Infected Pneumonia Monitored by Quantitative RT-PCR. J Korean Med Sci. 2020;35(6):e79. Epub 2020/02/15. doi: 10.3346/jkms.2020.35.e79. PubMed PMID: 32056407; PubMed Central PMCID: PMCPMC7025910.

53.   Wang Z, Chen X, Lu Y, Chen F, Zhang W. Clinical characteristics and therapeutic procedure for four cases with 2019 novel coronavirus pneumonia receiving combined Chinese and Western medicine treatment. Biosci Trends. 2020;14(1):64-8. Epub 2020/02/11. doi: 10.5582/bst.2020.01030. PubMed PMID: 32037389.

54.   Chen C, Zhang Y, Huang J, Yin P, Cheng Z, Wu J, et al. Favipiravir versus Arbidol for COVID-19: A Randomized Clinical Trial. medRxiv. 2020.

55.   Zhu Z, Lu Z, Xu T, Chen C, Yang G, Zha T, et al. Arbidol monotherapy is superior to lopinavir/ritonavir in treating COVID-19. J Infect. 2020. Epub 2020/04/14. doi: 10.1016/j.jinf.2020.03.060. PubMed PMID: 32283143; PubMed Central PMCID: PMCPMC7195393.

56.   Lian N, Xie H, Lin S, Huang J, Zhao J, Lin Q. Umifenovir treatment is not associated with improved outcomes in patients with coronavirus disease 2019: a retrospective study. Clin Microbiol Infect. 2020. Epub 2020/04/29. doi: 10.1016/j.cmi.2020.04.026. PubMed PMID: 32344167; PubMed Central PMCID: PMCPMC7182750.

57.   Leneva IA, Russell RJ, Boriskin YS, Hay AJ. Characteristics of arbidol-resistant mutants of influenza virus: implications for the mechanism of anti-influenza action of arbidol. Antiviral Res. 2009;81(2):132-40. Epub 2008/11/26. doi: 10.1016/j.antiviral.2008.10.009. PubMed PMID: 19028526.

58.   Teissier E, Zandomeneghi G, Loquet A, Lavillette D, Lavergne JP, Montserret R, et al. Mechanism of inhibition of enveloped virus membrane fusion by the antiviral drug arbidol. PLoS One. 2011;6(1):e15874. Epub 2011/02/02. doi: 10.1371/journal.pone.0015874. PubMed PMID: 21283579; PubMed Central PMCID: PMCPMC3026800.

59.   Pécheur EI, Lavillette D, Alcaras F, Molle J, Boriskin YS, Roberts M, et al. Biochemical mechanism of hepatitis C virus inhibition by the broad-spectrum antiviral arbidol. Biochemistry. 2007;46(20):6050-9. Epub 2007/04/26. doi: 10.1021/bi700181j. PubMed PMID: 17455911; PubMed Central PMCID: PMCPMC2532706.

60.   Barik A, Rai G, Modi G. Molecular docking and binding mode analysis of selected FDA approved drugs against COVID-19 selected key protein targets: An effort towards drug repurposing to identify the combination therapy to combat COVID-19. arXiv. 2020. doi: arXiv:2004.06447v1.

61.   Vankadari N. Arbidol: A potential antiviral drug for the treatment of SARS-CoV-2 by blocking trimerization of the spike glycoprotein. Int J Antimicrob Agents. 2020:105998. Epub 2020/05/04. doi: 10.1016/j.ijantimicag.2020.105998. PubMed PMID: 32360231; PubMed Central PMCID: PMCPMC7187825.

Table 1. Comparison of the binding free energy and various energy components between Arbidol-ACE2 and Arbidol-RBD from MD simulation trajectory.
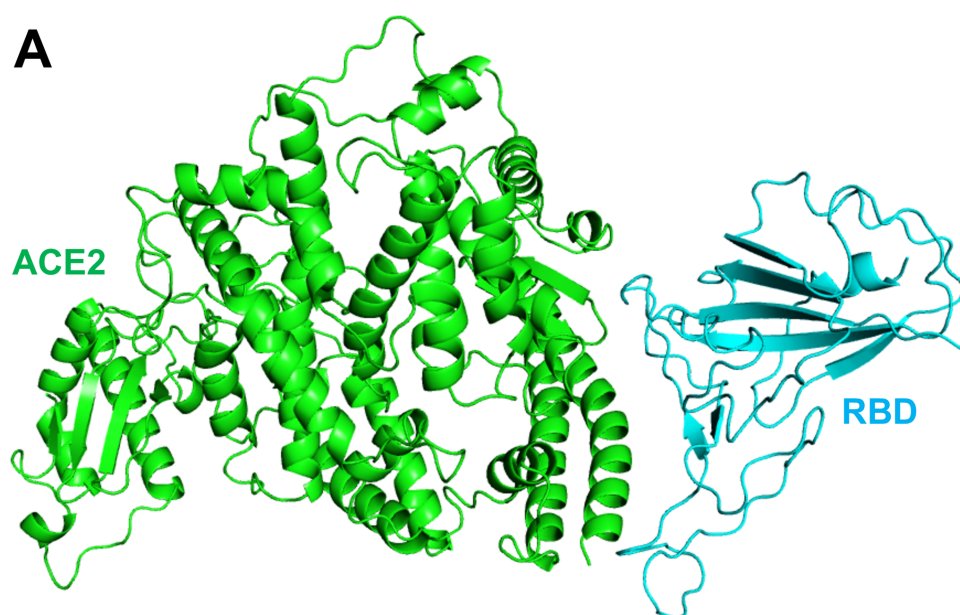
Energy components	Arbidol-ACE2 (kJ/mol)	Arbidol-RBD (kJ/mol)
Van der Waal energy	-188.07 ± 7.67	-190.87 ± 1.78
Electrostatic energy	-7.03 ± 3.09	-35.82 ± 2.91
Polar solvation energy	41.48 ± 15.69	49.67 ± 14.32
SASA energy	-16.04 ± 1.44	-17.13 ± 0.68
Binding energy	-169.66 ± 15.88	-194.16 ± 11.88

Table 2. PRODIGY-derived decomposition of intermolecular contacts for the apo-RBD/ACE2 complex and RBD/ACE2-Arbidol complex from the last 30 ns MD simulation trajectories.
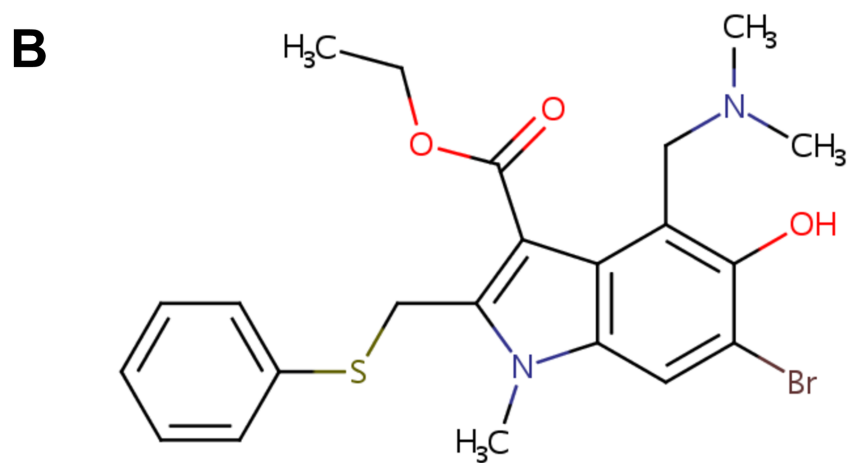
Types of contacts	Apo-RBD/ACE2 complex	Types of contacts	RBD/ACE2-Arbidol complex
No. of intermolecular contacts	59	No. of intermolecular contacts	74
No. of charged-charged contacts	1	No. of charged-charged contacts	1
No. of charged-polar contacts	9	No. of charged-polar contacts	13
No. of charged-apolar contacts	18	No. of charged-apolar contacts	23
No. of polar-polar contacts	4	No. of polar-polar contacts	3
No. of apolar-polar contacts	18	No. of apolar-polar contacts	18
No. of apolar-apolar contacts	9	No. of apolar-apolar contacts	16
% of apolar NIS residues	35.58	% of apolar NIS residues	34.94
% of charged NIS residues	26.76	% of charged NIS residues	27.71
Predicted binding affinity (kcal/mol)	-10.8	Predicted binding affinity (kcal/mol)	-11.5

Table 3. PPCheck-derived energy components for the apo-RBD/ACE2 complex and RBD/ACE2-Arbidol complex from the last 30 ns MD simulation trajectories.
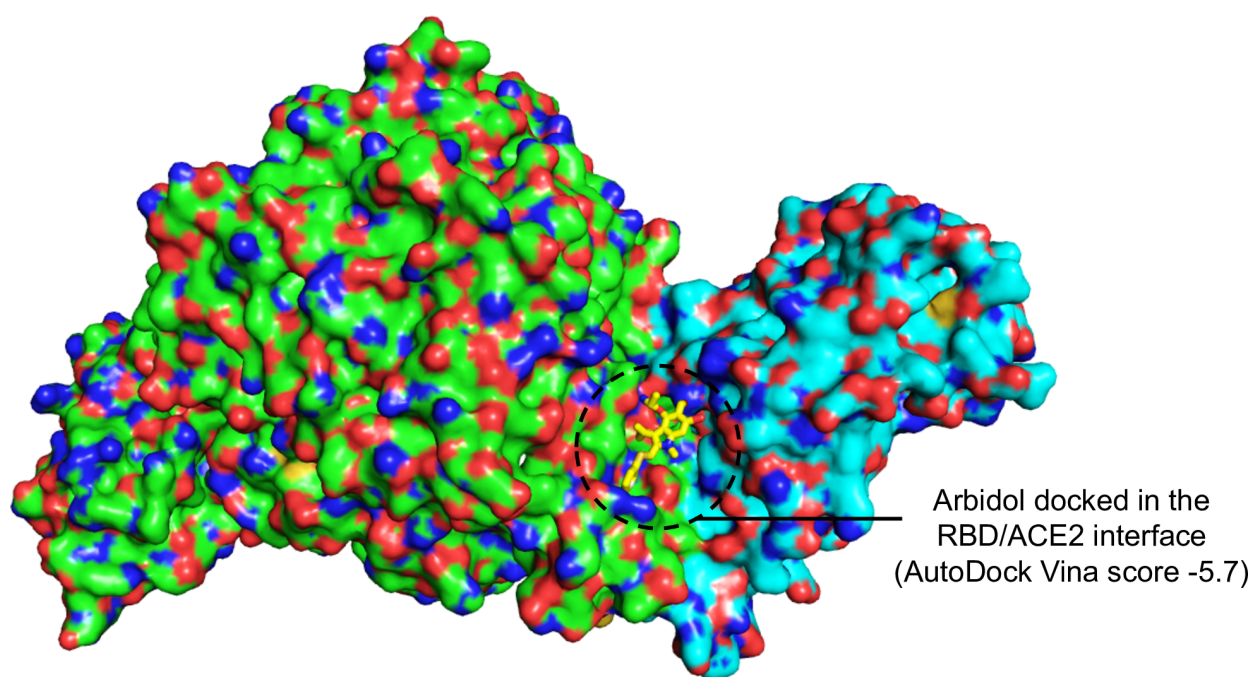
Energy components	Apo-RBD/ACE2 complex	RBD/ACE2-Arbidol complex
Hydrogen bond energy	-7.56 kJ/mol	-8.43 kJ/mol
Electrostatic energy	-1.92 kJ/mol	10.22 kJ/mol
van der Waals energy	-103.99 kJ/mol	-173.35 kJ/mol
Total stabilizing energy	-113.46 kJ/mol	-171.57 kJ/mol
No. of interface residues	75	74
Normalized energy per residue	-1.51 kJ/mol	-2.32 kJ/mol
No. of short contacts	0	2
No. of hydrophobic interactions	1	3
No. of van der Waals Pairs	1915	2595
No. of Salt Bridges	0	0
No. of Potential Favourable Electrostatic Interactions	1	0
No. of Potential Unfavourable Electrostatic Interactions	1	2

A

ACE2

RBD

ACE2-RBD complex of SARS-CoV-2

B
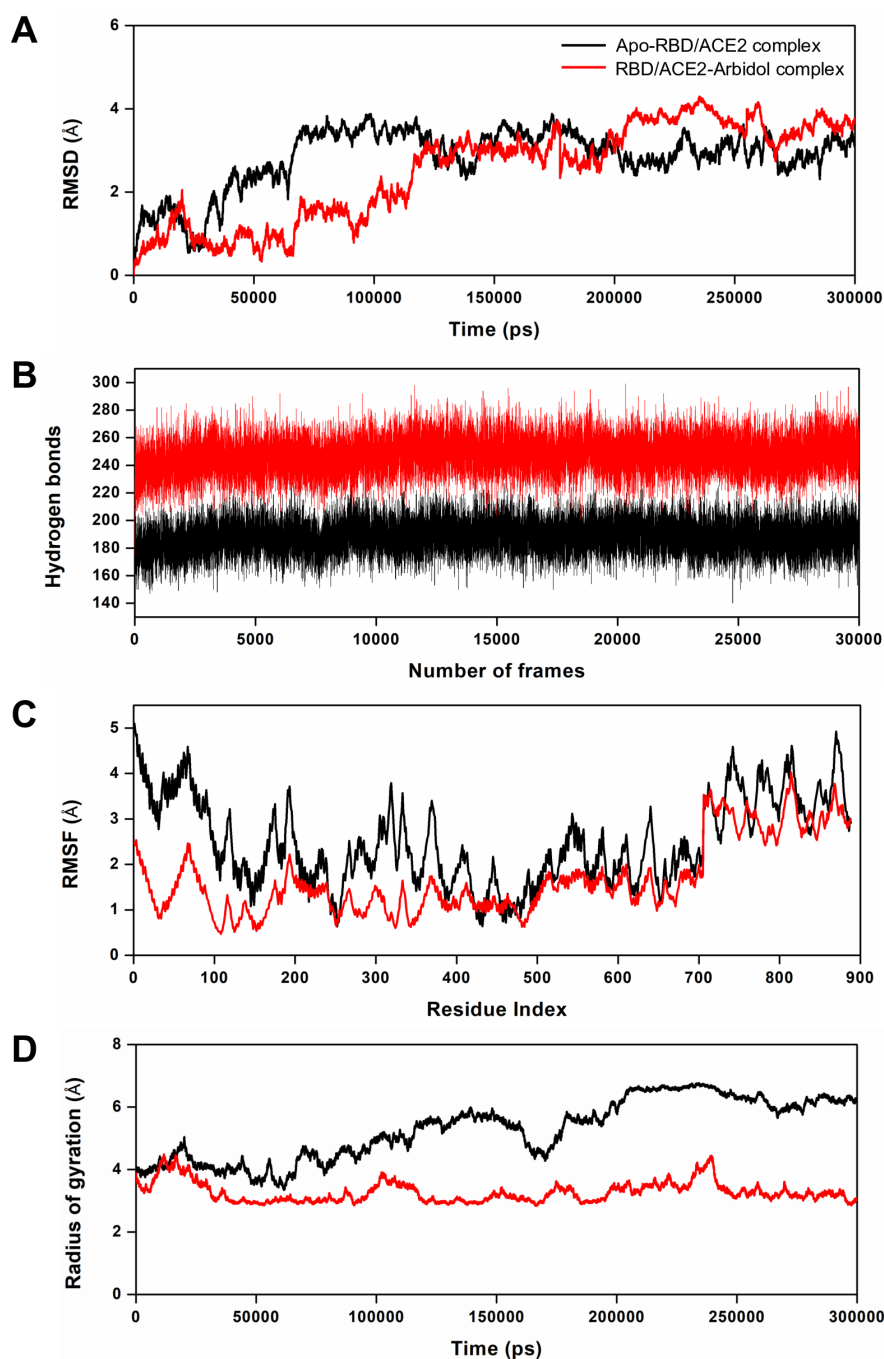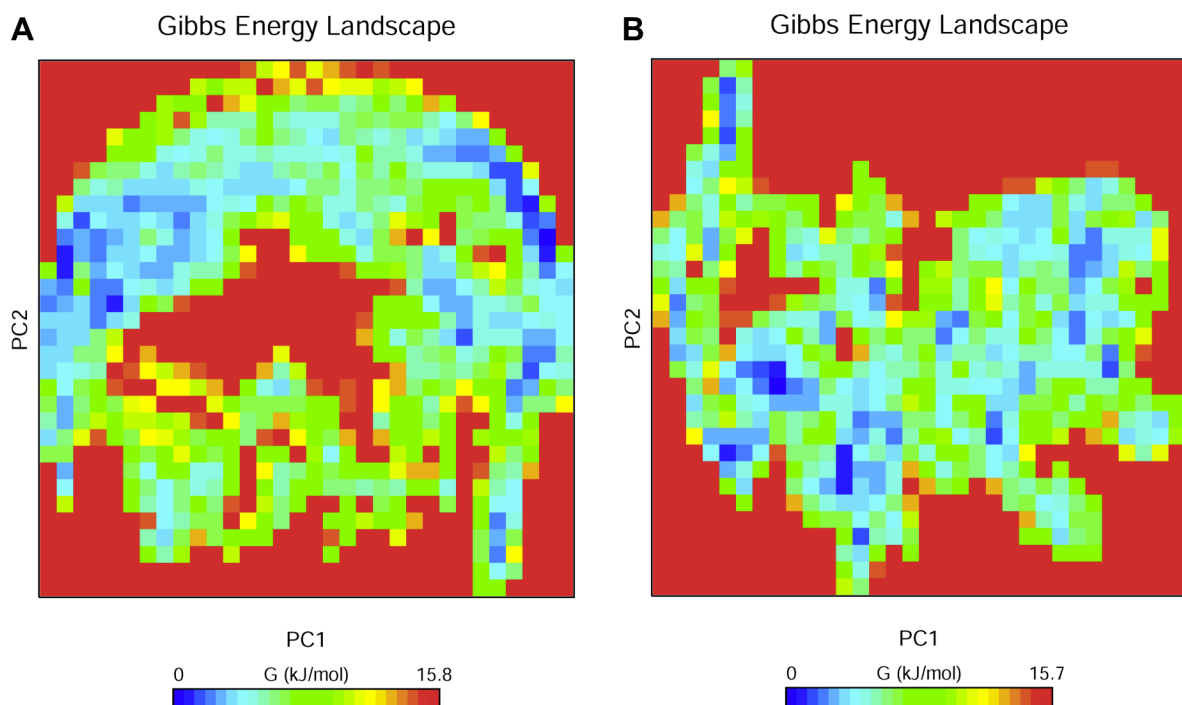
Arbidol

Fig 1. Representation of ACE2/RBD complex and Arbidol. (A) Ribbon structure of ACE2/RBD complex (ACE2: green and RBD: cyan) showing the interface, (B) 2D structural representation of Arbidol.

Arbidol docked in the
RBD/ACE2 interface
(AutoDock Vina score -5.7)

Fig 2. Docked pose of Arbidol into ACE2/RBD interacting interface. (A) Surface representation of ACE2/RBD interface showing the docked site of Arbidol, (B) AutoDock Vina score showing the docked score and other details of the molecular docking results.
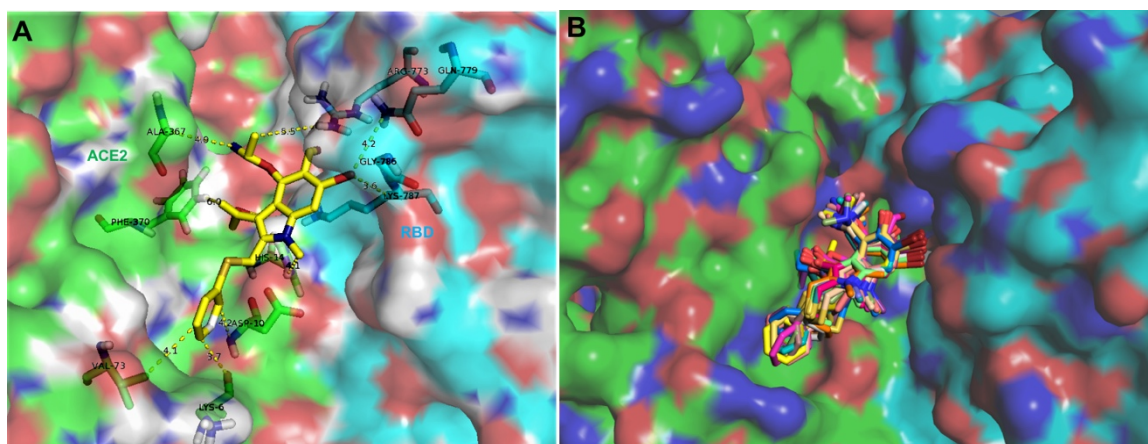
Fig 3. MD simulation derived structural and dynamic parameters from apo-RBD/ACE2 complex and RBD/ACE2-Arbidol complex. (A) Plots showing the backbone RMSD profiles of apo-RBD/ACE2 complex and RBD/ACE2-Arbidol complex during the course of MD simulations, (B) The total number of hydrogen bonds formed during the 300 ns simulations for both complexes.
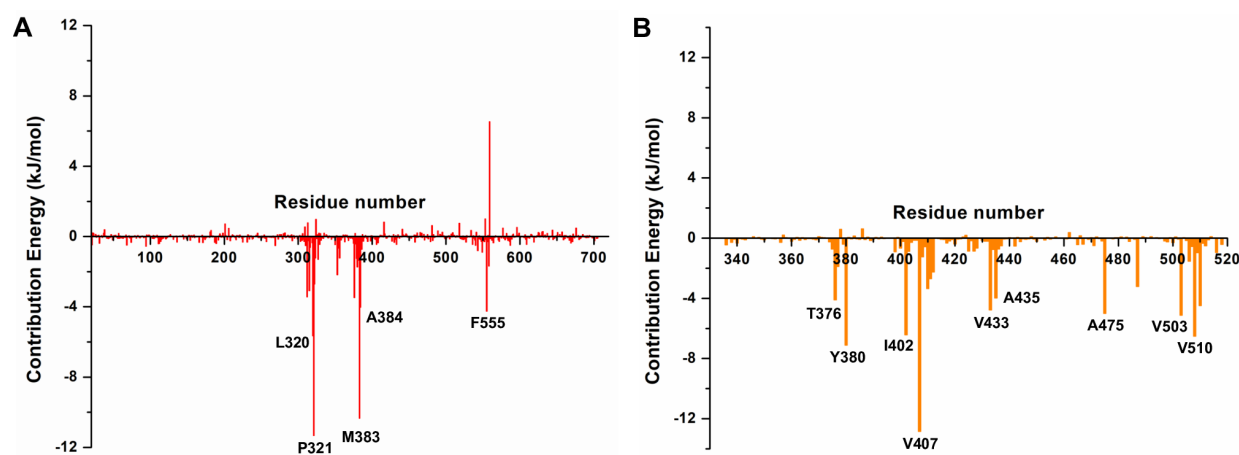
Fig 4. Free energy landscapes of apo-RBD/ACE2 complex and RBD/ACE2-Arbidol complex. The free energy landscapes generated by projecting the principal components, PC1, and PC2, of (A) apo-RBD/ACE2 complex, and (B) RBD/ACE2-Arbidol complex from MD simulations at 300 K. The free energies are represented by $-k_B T \ln P_{(PC1, PC2)}$ with $P_{(PC1, PC2)}$ being the distribution probability calculated using the structures sampled at 300 K. The blue, green, and cyan color represent metastable conformations with low-energy states, while red color signifies the high-energy protein conformations.

Fig 5. Molecular interaction of Arbidol with RBD/ACE2. (A) A 3D interaction diagram showing the contacts and interactions of Arbidol with RBD/ACE2 complex residues during MD simulations. The bond lengths are shown as dashed lines, and the distances are labeled, (B) Superimposed structures of Arbidol in the RBD/ACE2 complex over the last 30 ns MD simulation of RBD/ACE2-Arbidol complex.

Fig 6. Contribution energy of the ACE2 and RBD residues towards Arbidol. (A) The per-residue energy contribution of (A) ACE2, and (B) RBD residues, towards Arbidol binding as obtained from the MM-PBSA binding affinity calculations.